Photoinduced hole hopping through tryptophans in proteins

Stanislav Záliš[a,*], Jan Heyda[a,b], Filip Šebesta[c], Jay R. Winkler[d], Harry B. Gray[d,*], Antonín Vlček[a,c,*]

[a] J. Heyrovský Institute of Physical Chemistry, Academy of Sciences of the Czech Republic, Dolejškova 3, CZ-182 23 Prague, Czech Republic
[b] Department of Physical Chemistry, University of Chemistry and Technology, Prague, Technická 5, CZ-166 28 Prague, Czech Republic
[c] School of Biological and Chemical Sciences, Queen Mary University of London, Mile End Road, London E1 4NS, United Kingdom
[d] Beckman Institute, California Institute of Technology, Pasadena, California 91125, United States

ORCID:
Jan Heyda: 0000-0002-9428-9508
Harry B. Gray: 0000-0002-7937-7876
Filip Šebesta: 0000-0001-6707-8118
Antonín Vlček: 0000-0002-6413-8311
Jay R. Winkler: 0000-0002-4453-9716
Stanislav Záliš: 0000-0003-4345-3205

Corresponding Author for PNAS: Harry B. Gray, Beckman Institute, California Institute of Technology, Pasadena, California 91125, hbgray@caltech.edu Assuming contributed mode of submission.

The authors declare no conflict of interest.

Author contributions:
S.Z., J.H., A.V. designed the research, S.Z., J.H., F.Š. carried out the research, S.Z., J.H., F.Š., J.R.W., H.B.G., A.V. analyzed and interpreted results, H.B.G. and A.V. wrote the paper.

Classification:
Major: Physical Sciences
Minor: Chemistry and Biophysics and Computational Biology

Keywords:
electron transfer, hole hopping, azurin, tryptophan, TDDFT, molecular dynamics

Abstract

Hole hopping through tryptophan/tyrosine chains enables rapid unidirectional charge transport over long distances. We have elucidated structural and dynamical factors controlling hopping speed and efficiency in two modified azurin constructs that include a rhenium(I) sensitizer, $Re(His)(CO)_3(dmp)^+$, and one or two tryptophans (W_1, W_2). Experimental kinetics investigations showed that the two closely spaced (3-4 Å) intervening tryptophans dramatically accelerated long-range electron transfer (ET) from Cu^I to the photoexcited sensitizer. In our theoretical work, we found that TDDFT QM/MM/MD trajectories of low-lying triplet excited states of $Re^I(His)(CO)_3(dmp)^+–W_1(–W_2)$ exhibited crossings between sensitizer-localized (*Re) and charge-transfer [$Re^I(His)(CO)_3(dmp^{\bullet-})/(W_1^{\bullet+}$ or $W_2^{\bullet+})$] (CS1 or CS2) states. Our analysis revealed that the distances, angles, and mutual orientations of ET-active cofactors fluctuate in a relatively narrow range in which the cofactors are strongly coupled, enabling adiabatic ET. Water-dominated electrostatic field fluctuations bring *Re and CS1 states to a crossing where $*Re(CO)_3(dmp)^+ \leftarrow W_1$ ET occurs and CS1 becomes the lowest triplet state. ET is promoted by solvation dynamics around $*Re(CO)_3(dmp)^+(W_1)$; and CS1 is stabilized by $Re(dmp^{\bullet-})/W_1^{\bullet+}$ electron/hole interaction and enhanced $W_1^{\bullet+}$ solvation. The second hop, $W_1^{\bullet+} \leftarrow W_2$, is facilitated by water fluctuations near the W_1/W_2 unit, taking place when the electrostatic potential at W_2 drops well below that at $W_1^{\bullet+}$. Insufficient solvation and reorganization around W_2 makes $W_1^{\bullet+} \leftarrow W_2$ ET endergonic, shifting the equilibrium toward $W_1^{\bullet+}$ and decreasing the charge-separation yield. We suggest that multiscale TDDFT/MM/MD is a suitable technique to model the simultaneous evolution of photogenerated excited-state manifolds.

Significance Statement

Electron (hole) hopping through tryptophan residues activates protein cofactors, participates in cellular photo-signaling, and protects enzymes from oxidative degradation. The energetics of excited chromophores together with their positions relative to proximal indoles are evolution-optimized in natural photolyases and cryptochromes. Our theoretical analysis of photoinduced hole hopping through tryptophans in rhenium-modified blue copper proteins has shed new light on the roles of electronic coupling and adiabaticity, as well as electrostatic-field fluctuations and solvation dynamics in driving charge transport rapidly over long distances. The take home message is that attention should be paid to solvation of redox-active molecules in hopping chains in the design of bioinspired light-harvesting systems and functional photocatalysts.

Introduction

Electron (hole) transport along chains of tryptophan (W) and tyrosine (Y) residues in proteins (1, 2) plays an essential role in delivering reducing or oxidizing equivalents to active sites in enzymes (ribonucleotide reductase (3-7), photolyase (PL) (8-15), cytochrome *c* peroxidase (16-18), methylamine utilization protein MauG (19), laccases (20-22), respiratory complex I (23) signaling (cryptochromes, CRY (8, 13, 24)), as well as in protecting oxidases from self-damage (20, 25-27) by transporting high-potential holes to the protein surface where they can be disarmed by cellular reductants. It also is likely that electron hopping through multiheme bacterial cytochromes is responsible for reduction of extracellular mineral acceptors (28-31), whereas chains of FeS clusters carry electrons, for example, in the respiratory Complex I (32, 33) and hydrogenases (34). Nearly all these processes are thought to involve nonadiabatic electron-tunneling steps between W, Y, heme, or FeS-cluster sites.

To investigate the factors controlling multistep electron tunneling (hole hopping), we covalently attached a $Re^{I}(CO)_3(dmp)^+$ photooxidant (abbreviated Re; dmp = 4,7-dimethyl-1,10-phenanthroline) to surface histidines H124 or H126 in the blue copper protein *Pseudomonas aeruginosa* azurin, and engineered an artificial hopping pathway by inserting one or two tryptophan residues between the Re and Cu^{I} sites, affording mutants ReH124W122 (**Re124W**) (35) and ReH126W124W122 (**Re126WW**) (36). Near-UV excitation of the appended Re complex triggered hole hopping through tryptophan(s), ultimately oxidizing the Cu^{I} site (Scheme 1) (35-39). While similar in operation to natural photoenzymes such as PLs and CRYs, **Re124W** or **Re126WW** show important quantitative differences whose understanding will help designing protein-based photocatalysts, solar-energy harvesting systems, and bioelectronic devices.

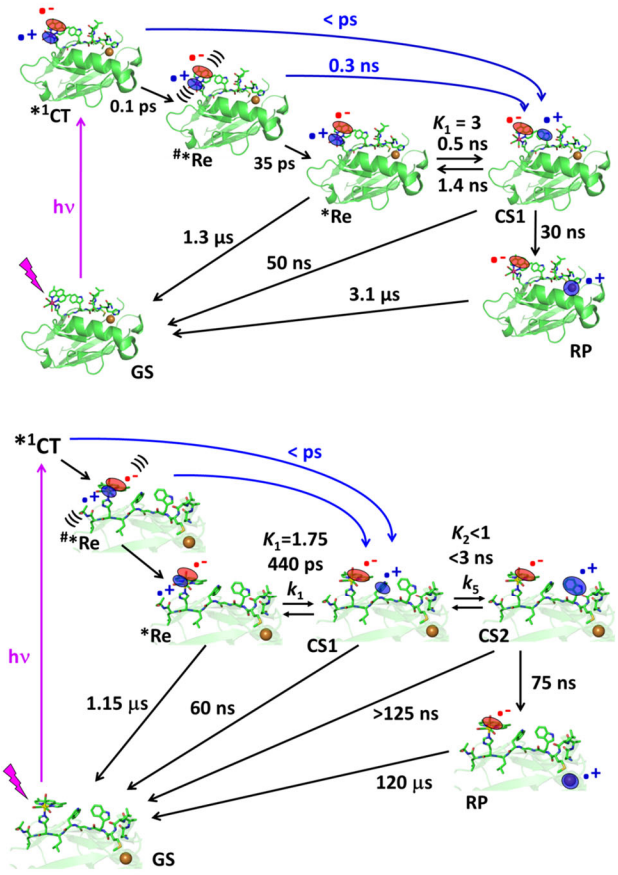

Scheme 1. Phototriggered electron transport in **Re124W** (35, 37) and **Re126WW** (36, 38) Cu^{I} azurins. Optical excitation of the Re complex to the ^{1}MLCT state is followed (39, 40) by ~150 fs ISC to hot triplet state(s) $^{\#}$*Re that undergo ps relaxation to the lowest triplet state *Re of mixed charge transfer ($Re(CO)_3 \rightarrow dmp$) / intraligand ($\pi\pi^*$-dmp) character (CT/IL). Electron transfer (ET) from the proximal tryptophan results in the charge-separated state (CS1) $Re^{I}(CO)_3(dmp^{\bullet-})(H124)(W122^{\bullet+})Cu^{I}$ or $Re^{I}(CO)_3(dmp^{\bullet-})(H126)(W124^{\bullet+})(W122)Cu^{I}$. In **Re124W** azurins, $Cu^{I} \rightarrow W122^{\bullet+}$ ET in CS1 produces the redox product (RP) $Re^{I}(CO)_3(dmp^{\bullet-})H124W122Cu^{II}$. The cycle is then closed by ~3 µs $dmp^{\bullet-} \rightarrow Cu^{II}$ back ET. In **Re126WW**, the CS1 state is converted to CS2 by $W124^{\bullet+} \leftarrow W122$ ET (the second hole "hop"). RP formation and ~120 µs back ET follow. Electron transport occurs over 19 (**Re124W**) and 23 Å (**Re126WW**).

Importantly, electron transport from Cu^{I} to the electronically excited Re complex (*Re) is 300× (**Re124W**) and 10,000× (**Re126WW**) faster than estimated for single-step hole tunneling over the same distances, although the much greater accelerating effect of two tryptophans

comes at the expense of a lower yield (36). Such a lower yield is not observed for PLs nor CRYs, where charge separation between the flavin chromophore and the surface Trp (or Tyr) occurs through two or three intervening tryptophans with a quantum yield of about 0.2 (12). We would like to know whether different protein and tryptophan solvation dynamics are responsible for the lower charge-separation efficiency in **Re126WW** compared to evolution-optimized natural photoenzymes. In addition, while ET from the proximal tryptophan to the photoexcited chromophore in all these systems (and in flavodoxins (41, 42)) is influenced by electronic coupling between aromatic rings, the ET time constants depend on the nature of the chromophore, ranging from 0.4-0.8 ps (CRYs) (10, 24) or 30-45 ps (PLs) (11, 12) to ca. 500 ps in Re-azurins.

Here we present results of a theoretical study designed to qualitatively understand roles of electronic states involved, their coupling, solvent/protein fluctuations that couple to hole hopping in **Re124W** and **Re126WW**, as well as the validity of the nonadiabaticity assumption. To this end, we have developed a multiscale QM/MM/MD procedure to calculate the temporal evolution of a manifold of low-lying excited states of the active part (Fig. 1) by TDDFT, while the dynamics of protein environment and water molecules are simulated classically. The simulations were performed in reactive *Re states of **Re124W** and **Re126WW** searching for conditions that would convert the systems to the CS1 product.

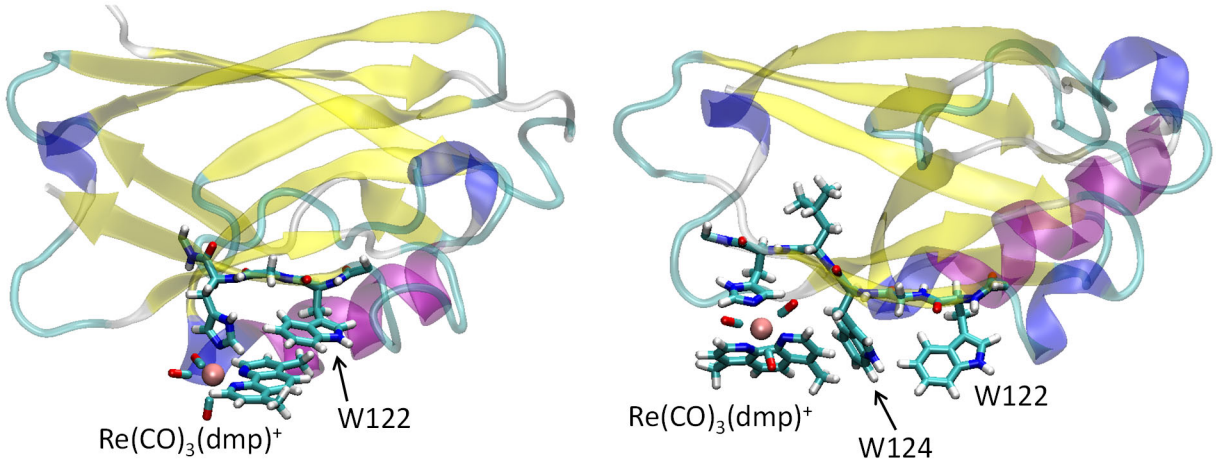

Fig. 1. Parts of **Re124W** (left) and **Re126WW** (right) azurins treated by quantum (QM, licorice representation) and molecular (MM, cartoon) mechanics. The QM parts consisted of $Re(CO)_3$(dmp)H124G123W122 and $Re(CO)_3$(dmp)H126L125W124G123W122 azurin fragments, respectively. The MM parts also included water molecules and the Cu^I atom (not shown).

Results and Discussion

Approach. We have modeled the conversion between the lowest triplet excited state (*Re) and the lowest CS1 state in **Re124W** and **Re126WW**. This conversion corresponds to the excited-state ET process responsible for ca. 90 % of the photoinduced charge separation between the Re complex and the proximal tryptophan, W122 or W124, respectively (35-37). Aiming at qualitative understanding ET-promoting structural and solvational dynamics, we have employed a multiscale QM/MM/MD procedure that describes the system in full, including explicit water and the protein environment (Fig. 1) and treating the active part at a TDDFT level with the PBE0 functional appropriate for systems containing a heavy-metal atom. To make these simulations computationally feasible, we performed Born-Oppenheimer (BO) dynamics. Although we have calculated several low-lying triplet excited states simultaneously, population of higher states around and behind the crossing region in BO dynamics was prevented by neglecting time evolution of the total electronic wave function together with the absence of nonadiabatic

couplings (43). We approximated the ET step by the two-state model (44, 45) and searched for conditions leading to the change of the lowest triplet state character from *Re to CS1. Calculations consisted of three steps:

1) *MM/MD* simulations of solution structures of both Re-azurins in their ground- (*SI Appendix*, Fig. S1) and lowest triplet excited states (*Re, Fig. 2 and *SI Appendix*, Fig. S3), using unique sets of realistic MM parameters for ground- and excited states of Re(imidazole)$(CO)_3$$(dmp)^+$ in the protein environment (derived in *SI Appendix*, section S13 and spectroscopically validated in *SI Appendix*, Fig. S2). Classical MM/MD excited-state trajectories, which modeled the "slow" evolution of the reacting system due to protein and solvent motion, provided a set of starting geometries and velocities for subsequent QM/MM/MD;

2) in the next step, we ran *UKS QM/MM/MD* simulations of the lowest triplet state starting from six different points at MM trajectories of each ***Re124W** and ***Re126WW**, denoted by capital letters in Fig. 2-top. UKS/MM/MD trajectories characterized the reactive state *Re (Fig. 2 and *SI Appendix* Figs. S5-S6), and adjusted the structure and solvation to the actual *Re charge distribution;

3) and from each of the UKS trajectories, we chose 2 or 3 snapshots serving as starting points for *TDDFT QM/MM/MD* trajectories that mapped the temporal evolution of a set of low-lying electronic states (Figs. 3, 4; all calculated trajectories in the *SI Appendix*, Figs. S7-S8).

For **Re124W**, we have calculated 12 TDDFT/MM/MD trajectories that all exhibited a *Re/CS1 state crossing. Out of the 17 calculated **Re126WW** trajectories, 9 showed *Re/CS1 crossings, one started in CS1, and 7 trajectories indicated a *Re/CS2 crossing. One trajectory (B-3) exhibited both *Re/CS1 and CS1/CS2 crossings, fortuitously providing insight into the second

hop, i.e. W124$^{\bullet+}$←W122 ET. TDDFT trajectories were then analyzed in terms of electronic coupling between the *Re and CS1 states, and accompanying structural/solvational changes. Emerging common patterns helped to unravel conditions promoting ET even in the absence of statistical evaluation, which was not possible, owing to computational-time demands of TDDFT/MM/MD.

Reactive excited state (*Re). The W122 indole and the dmp ligand in ***Re124W** are in two nearly stacked orientations with average angles of approximately 20 and 34°. In each conformation, they slightly fluctuate around their mean positions and an average closest C–C distance of 3.2 Å (Fig. 2-top, *SI Appendix*, Fig. S3). In ***Re126WW**, the W124 indole and dmp are mainly T-oriented (73±12°) with an average shortest distance of 3.45 Å. Rotations of $Re(CO)_3(dmp)^+$ around the Re–N(His126) bond at 27 and 31 ns reversibly switch the system to a short-lived conformation with dmp pointing away from the W124 indole, in which it spends 5.75% of the MD simulation time.

In agreement with previous work on $ReL(CO)_3$(polypyridyl) complexes (40, 46-51), UKS/MM/MD trajectories showed that *Re arises from a combination of $d\pi(Re(CO)_3)\rightarrow\pi^*(dmp)$ ^{3}CT and $\pi\rightarrow\pi^*(dmp)$ ^{3}IL (intraligand) excitations, roughly described as $Re^{II}(His)(CO)_3(dmp^{\bullet-})^+$ and $Re^{I}(His)(CO)_3(*dmp)^+$, respectively. Relative contributions of the ^{3}CT and ^{3}IL components fluctuate with time, making the *Re electronic structure time dependent. In particular, the excited electron stays in the π^*(dmp) orbital while hole (de)localization varies in time between dmp (^{3}IL) and $Re(CO)_3$ (^{3}CT).

This behavior was demonstrated by anticorrelated variations of Mulliken charge and spin (difference of α-, β-spin electron populations) on dmp and $Re(CO)_3$ along UKS/MM/MD trajectories (Fig. 2 and *SI Appendix*, Figs. S4-S6). In particular, the spin at dmp varies between 2 (for ^{3}IL) and ~1.2 [corresponding to predominant ^{3}CT character with a minor ^{3}IL contribution (^{3}CT/^{3}IL)]; and the spin at $Re(CO)_3$ varies between 0 and ~0.8. Charges vary simultaneously from about +0.4 at both $Re(CO)_3$ and dmp for ^{3}IL to ca. +0.8 and –0.15, respectively, for ^{3}CT/^{3}IL. Interestingly, some spin and charge delocalization to W122 is seen in ^{3}IL sections of most **Re124W** trajectories. All these features are displayed by trajectory L that switches from ^{3}CT/IL to mainly ^{3}IL around 1.5 ps (Fig. 2).

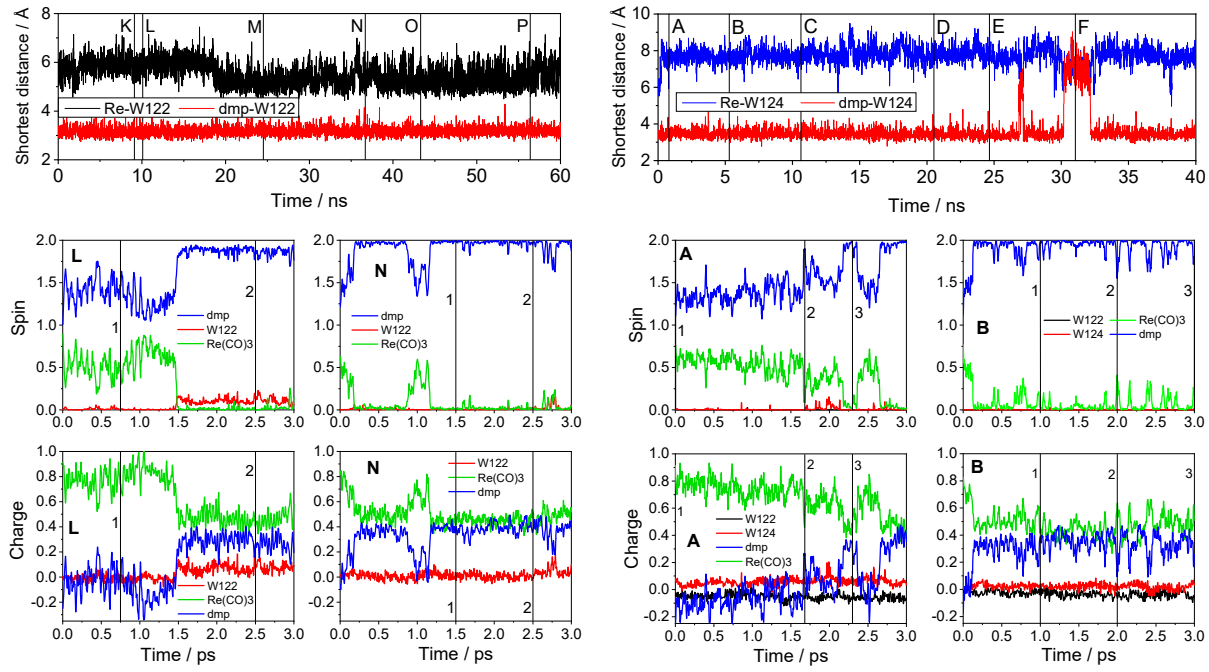

Fig. 2. Time evolution of the *Re state of **Re124W** and **Re126WW**. Top: classical MM trajectories of closest Re-indole (Re-C) and dmp-indole (C-C) distances calculated with *Re parametrization. Black vertical lines denote starting times for UKS dynamics. Second and third rows: Typical UKS/MM/MD spin and charge trajectories of the lowest triplet excited state (*Re) showing fluctuations between ^{3}CT and ^{3}IL character. Limiting ππ*(dmp) ^{3}IL is described by spin 0 at Re and 2 at dmp; limiting CT character by spin 1 at both dmp and $Re(CO)_3$. Numbered

vertical lines denote starting times for TDDFT/MM/MD simulations. Spin-density distributions in typical ^{3}CT/^{3}IL and ^{3}IL structures are displayed in *SI Appendix*, Fig. S4 and all calculated UKS trajectories in Figs. S5-S6.

***Re/CS1 crossing.** The time evolution of a manifold of low-lying triplet excited states were monitored by TDDFT/MM/MD; these states were characterized as *Re, CS1, or CS2 by Mulliken charges at the Re complex and the corresponding tryptophan indole(s). Individual trajectories differed by the starting snapshot taken from previously calculated UKS/MM/MD trajectories. Typical energy trajectories (Fig. 3) revealed the presence of several *Re-type states followed in energy by one or more CS1-type states. With time, CS1 state(s) underwent multiple crossings with other higher-lying states while decreasing in energy, then occasionally approached and finally crossed the trajectory of the lowest *Re state, becoming the lowest triplet state.

The *Re/CS1 crossing (i.e., the Re(His)$(CO)_3$(dmp)$^+$←W ET event) was clearly manifested on TDDFT/MM/MD trajectories following the charge distribution in the lowest triplet excited state (Fig. 4 and *SI Appendix*, Figs. S7-S8, S10), which showed a unit rise of the Mulliken charge at the indole and a concomitant drop at Re$(CO)_3$(dmp), in line with the Re^{I}(H124)(dmp$^{\bullet-}$)(W122$^{\bullet+}$) or Re^{I}(H126)(dmp$^{\bullet-}$)(W124$^{\bullet+}$)(W122) formulation of the CS1 state. The charge decrease on Re$(CO)_3$(dmp) was mostly localized at dmp if the switchover occurred from a *Re state of predominantly IL character (typically K-1, K-2, M-2, N-1, N-2, B-2, C-2, C-3) or delocalized over both Re$(CO)_3$ and dmp if there was substantial CT character in *Re (L-1, M-1, O-1, O-2, P-1, P-2, A-1, A-3, B-3, D-1). Interestingly, including 20 nearest water molecules into the QM space caused the A-1 *Re/CS1 crossing to take place ~20 fs earlier. Charges at individual water molecules fluctuated randomly in a narrow range and changes of charges at O-

atoms indicated only small electronic polarization of the H_2O molecules closest to the indole N-H groups in response to the *Re→CS1 conversion (*SI Appendix*, Fig. S10).

After the crossing, both proteins were stable in their CS1 states, in agreement with the finding (35) that *Re←W ET is slightly exergonic (~30 meV; K ≅ 3 for **Re124W**) and the second "hop" producing CS2 in **Re126WW** is slower (36). *Re/CS1 crossings and a stable CS1 were detected also on trajectories obtained with different computational protocols and/or using the CAM-B3LYP functional (*SI Appendix*, section S6).

Calculated *Re/CS1 crossing times varied between trajectories but they all fell within the first 2.5 ps. Experimentally, *Re←W ET is a multiphase process whose kinetics were fitted with ca. 300 and 500 ps time constants attributed to reactions from hot and (nearly) relaxed *Re, respectively (Scheme 1) (35). The difference between calculated crossing and experimental ET times is caused by TDDFT/MM/MD simulations starting in configurations close to the transition state. The simulated system contained some extra energy released upon the transition from MM to UKS and then from UKS to TDDFT, some of which could have been deposited in ET-enabling modes, above the *Re energy minimum. Given the low height of the reaction barrier (0.19 eV, estimated from Marcus theory), it is highly probable that TDDFT/MM/MD starting points were placed close to the top of the barrier and the trajectories monitored mostly fast ET-driving modes. This argument can be recast in the spirit of the Sumi-Marcus model (52, 53), whereby slow system evolution (solvent, protein) is modeled classically (MM/MD), while reaction along the "fast" coordinate (some fast solvent motions, intra-cofactor vibrations, *SI Appendix*, section S12) is sampled by TDDFT/MM/MD trajectories starting from randomly chosen points on the "slow" coordinate.

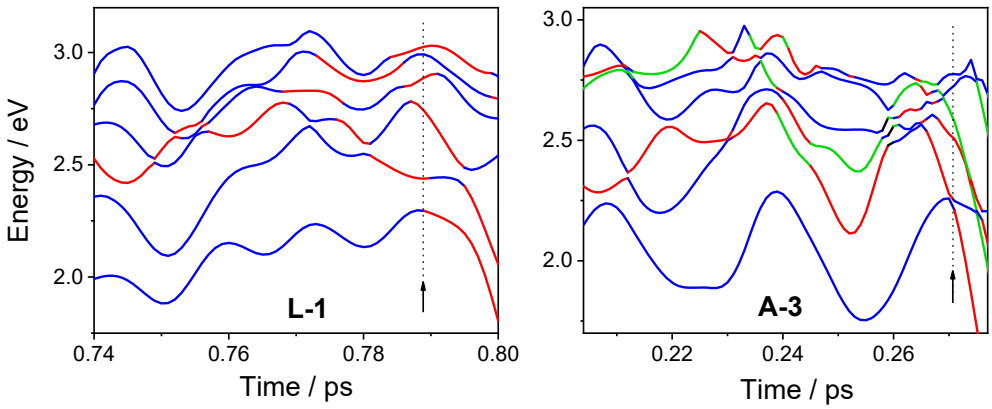

Fig. 3. TDDFT energy trajectories of the six lowest triplet excited states of **Re124W** (L-1) and **Re126WW** (A-3) in the proximity of *Re/CS1 crossing. (Behavior over a longer 0.3 ps interval is shown in *SI Appendix*, Fig. S9.) Blue: Re(imidazole)$(CO)_3$$(dmp)^+$ – localized *Re-type states defined by >0.5 total charge on the Re complex; Red: states with predominant CS1 character defined by >0.5 total charge on the proximal indole. Green: states with predominant CS2 character defined by >0.5 total charge on the W122 indole in **Re126WW**. Arrows and dotted vertical lines denote the calculated crossing times.

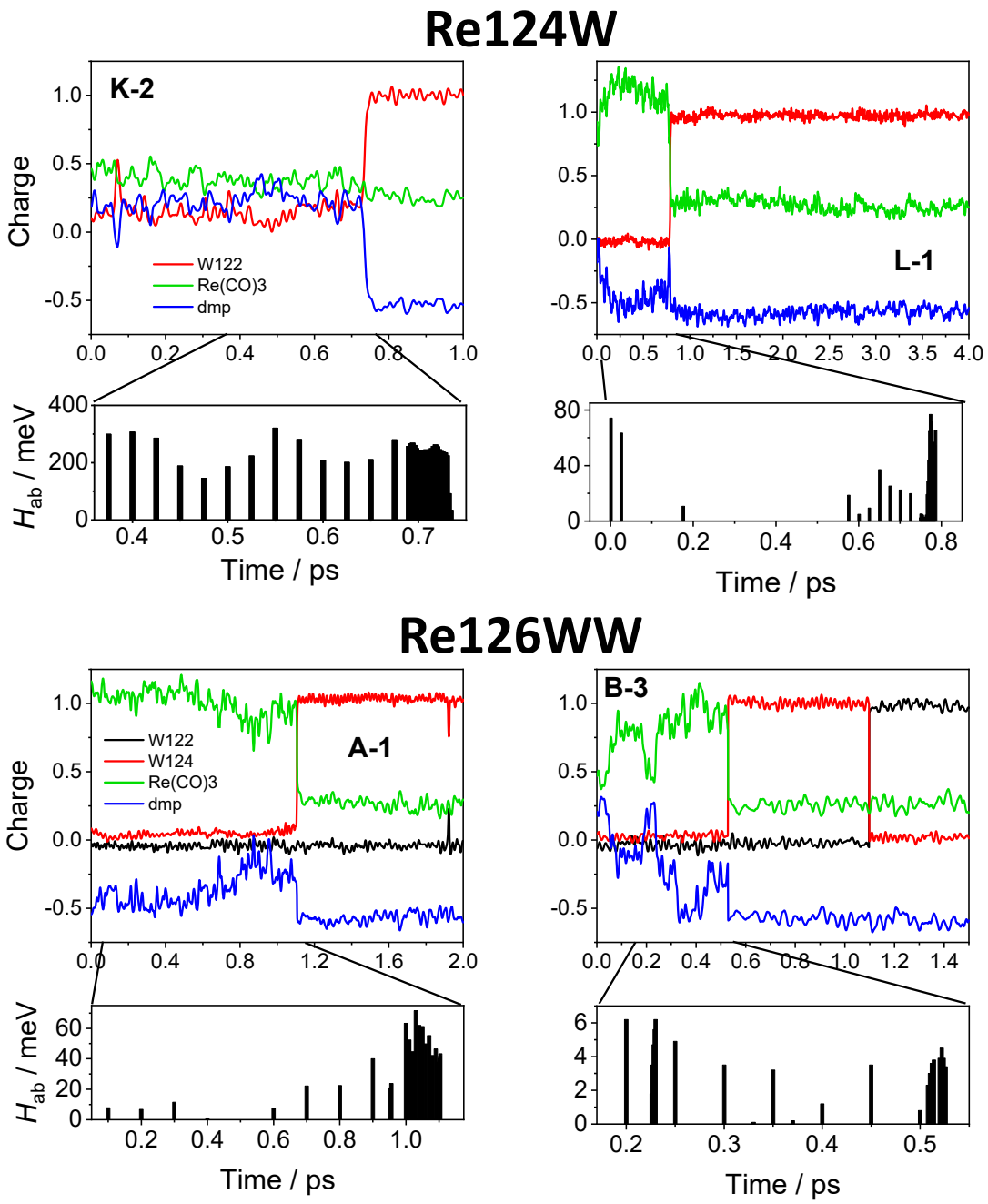

Fig. 4. Typical TDDFT/MM/MD charge trajectories of the lowest triplet excited state and *Re-CS1 electronic coupling. Changes in the charge distribution between $Re(CO)_3$ and dmp manifest changing *Re electronic structure caused by varying ^{3}IL and ^{3}CT contributions. Vertical jumps signify *Re/CS1 crossings (*i.e.* $*Re(CO)_3(dmp)^+ \leftarrow W$ ET), after which the charge distribution stabilizes in the CS1 state. B-3 exhibits also a CS1/CS2 crossing ($W124^{\bullet+} \leftarrow W122$ second "hop"). Black histograms show electronic couplings between the lowest *Re and the lowest CS1 states up to their crossing; the last bar occurs approximately at the time corresponding to ~1/2 of the charge jump. X-# trajectory notation: X = MM starting point; # = UKS starting point. All calculated trajectories and couplings are displayed in *SI Appendix*, Figs. S7-S8 and S13-S14.

Electronic coupling. Avoided crossing between the lowest *Re and CS1 states on TDDFT trajectories demonstrated that dynamical fluctuations of solvated Re-tryptophan-azurins create situations where oxidation of the proximal tryptophan by an electronically excited Re complex is energetically feasible, leading to a localized CS1 state. Calculating electronic coupling H_{ab} between their diabatic approximates in the crossing region enabled us to assess whether the studied ET approaches the adiabatic or nonadiabatic limit (45, 53-55) and, thus, whether a strong ET rate dependence on $|H_{ab}|$ should be expected. We employed the GMH/FCD method (56-58) to estimate transformation to the diabatic representation revealing strong coupling for most trajectories (Figs. 4, and *SI Appendix*, Figs. S13, S14), with rms values of 60 (**Re124W**) and 20 meV (**Re126WW**) at the tops of activation barriers (crossing points in the diabatic representation), with a large spread between trajectories: 13.2 – 97.0 and 0.1 – 41.7 meV, respectively; the more strongly coupled ones occurred more frequently (*SI Appendix*, Tabs. S1, S2); and even larger values were occasionally calculated at earlier times before crossings.

Coupling variations between and along trajectories result from a combination of electronic and steric effects. Larger $|H_{ab}|$ values calculated for **Re124W** than **Re126WW** reflect different indole/dmp relative positions: stacked (parallel-displaced, PD) and T-oriented, respectively. For each species, coupling was larger when *Re had more ^{3}IL character (K-1, K-2, M-2) as compared to ^{3}CT/^{3}IL (O-1, O-2, P-2). A similar trend was seen for **Re126WW**, where strongly coupled B-2 and C-2 had essentially ^{3}IL character before the crossing, whereas the only two weakly coupled cases B-1 and D-3 exhibited large charge fluctuations toward ^{3}CT in the crossing region. In some cases, both the IL contribution to the reacting *Re state and H_{ab}

increased as the trajectory approached the crossing (L-1, P-1, A-1). Pronounced fluctuations increasing ^{3}CT character on C-3 at ~0.31 and 0.615-0.665 ps were accompanied by markedly lower H_{ab} values compared to the rest of the trajectory, where *Re was predominantly ^{3}IL. Changes in the excited-state character alone cannot explain all coupling variations and must be considered together with geometric factors, namely, the indole–dmp distance, as well as the angle between the aromatic planes (*SI Appendix*, Tables S1, S2, Figs. S15, S16, and discussion in section S8). In general, strong coupling in **Re124W** was favored by a 20–30° tilt and by the indole benzene ring lying above dmp C5–C6 or C3–C4 bonds (central and side rings, respectively, *SI Appendix*, Fig. S15). The dependence on the closest distance was rather weak, observable only for trajectories with the same *Re character (e.g., M-2, N-2, N-1). In **Re126WW**, strong coupling occurred in cases where the indole was positioned sideways and nearly parallel to the C7–C8 bond of the dmp side ring (*SI Appendix*, Fig. S16), and the angle between the two aromatic planes deviated from an ideal 90° T-configuration to ~75°. The coupling dependence on the dmp/indole geometry as well as on the *Re electronic structure likely reflects changes in the frontier-orbital overlap involved in ET (indole HOMO, dmp-localized LUMO, LUMO+1, and low-lying π orbitals that are depopulated upon ^{3}IL excitation, *SI Appendix*, Figs. S17, S18).

Adiabaticity. Although average H_{ab} values predict *Re(CO)$_3$(dmp)$^+$←W ET in ***Re126WW** to be ~10× slower than in ***Re124W**, comparable rates (~500 ps)$^{-1}$ were determined experimentally for both species (Scheme 1) (35-38), as well as for similar interfacial ET in **Re126T124W122** (59). These observations, together with the relatively large $|H_{ab}|$ values, suggest that ET is adiabatic,

largely controlled by the effective frequency of nuclear motion along the reaction coordinate, ν_{eff}. Indeed, using the average coupling values and a typical (2, 35) reorganization energy λ = 0.8 eV, *Re(CO)$_3$(dmp)$^+$←W ET does not meet the nonadiabaticity condition requiring the Landau-Zener parameter $2\pi\gamma = \pi^{3/2}\langle H_{ab}^2\rangle/h\nu_{eff}\sqrt{(\lambda k_B T)}$ to be << 1 (45, 60), unless ν_{eff} is unrealistically large [$2\pi\gamma$ of 0.1 would require $\nu_{eff} = 3.4\times10^{14}$ s^{-1} (11360 cm^{-1}) for **Re124W** or 3.8×10^{13} s^{-1} (1260 cm^{-1}) for **Re126WW]**. The same conclusion can be reached in a medium-fluctuation controlled regime (54, 55) where the adiabaticity contribution is estimated using a parameter $\kappa = 4\pi H_{ab}^2\langle\tau\rangle/\hbar\lambda$, where $\langle\tau\rangle$ is the medium relaxation time induced by a constant charge distribution (54, 55, 61). Setting $\kappa \geq 1$ as a limit for an adiabatic reaction would require $\langle\tau\rangle \geq 12$ fs for ***Re124W** and ≥ 100 fs for ***Re126WW**, using rms H_{ab} values of 60 and 20 meV, respectively. Relaxation times indicated by electrostatic-potential trajectories (200-600 fs, discussed below) and time-resolved spectroscopic experiments (pico/nanoseconds, (48, 62) lie well above these limits, supporting the conclusion of *Re(CO)$_3$(dmp)$^+$←W ET adiabaticity. (These adiabaticity arguments are valid over a broad range of λ values, approximately for λ < 2.5 eV. In addition, trajectories with above-average $|H_{ab}|$ values can be expected to dominate the process, further lowering the upper limits of relaxation times.)

Water distribution. Solvation of the W122-indole in ***Re124W** and W124-indole (***Re126WW**) strengthened along TDDFT/MM/MD trajectories as the system approached the *Re/CS1 crossing region, becoming CS1-like shortly before the actual crossing. This behavior indicated

that water fluctuations around indole facilitate *Re(CO)$_3$(dmp)←W ET by driving the system in the direction of the CS1 product.

We have quantified solvation by a water proximal radial distribution function g(*r*) (63, 64) calculated around the indole(s) and averaged over relevant sections of trajectories showing a *Re/CS1 crossing (*SI Appendix*, Fig. S19). The g(*r*) around W122 in ***Re124W** or W124 in ***Re126WW** peaked below 2.0 Å due to water molecule(s) H-bonded to the indole N–H group, followed by a broad maximum (second solvation layer) at 2.5–3.2 Å, Fig. 5. The g(*r*) calculated over a 20 fs interval before the *Re/CS1 crossing was either shifted closer to the indole (W122 in ***Re124W**) or the first peak sharpened and increased in intensity (W124 in ***Re126WW**), resembling in each case g(*r*) averaged over CS1 regions after the crossing. In the both cases, the ratio of g(*r*) magnitudes at the first maximum and the following minimum was higher during 20 fs before the crossing and in the CS1 region compared to the *Re average, indicating (65, 66) that solvating water molecules become more strongly H-bonded to the indole and partly disconnected from the second solvation layer just before the crossing (this situation continues in the CS1 product). Gradual "tightening" of indole solvation on approach to the *Re/CS1 crossing also is manifested by g(*r*) calculated over subsequent 100 fs intervals along averaged trajectories as well as single A-1 trajectory (*SI Appendix*, Fig. S20). Solvation of the distal W122 indole in ***Re126WW** also strengthens upon *Re/CS1 conversion (Fig. 5-bottom), suggesting that emergence of the positive charge at W124 attracts water molecules to the entire W124···W122 region. However, the W122 indole was always solvated less and more weakly H-bonded than W124, as documented by the first g(*r*) maximum occurring ~0.1 Å farther and by a smaller max/min ratio. Space-filling models (Fig. 5) revealed that W122 in either system is much

less water-exposed than W124, being partly shielded by a L120A119S118 α-helix whose A119 backbone oxygen atom occasionally becomes H-bonded to the NH group (*SI Appendix*, Figs. S21, S22).

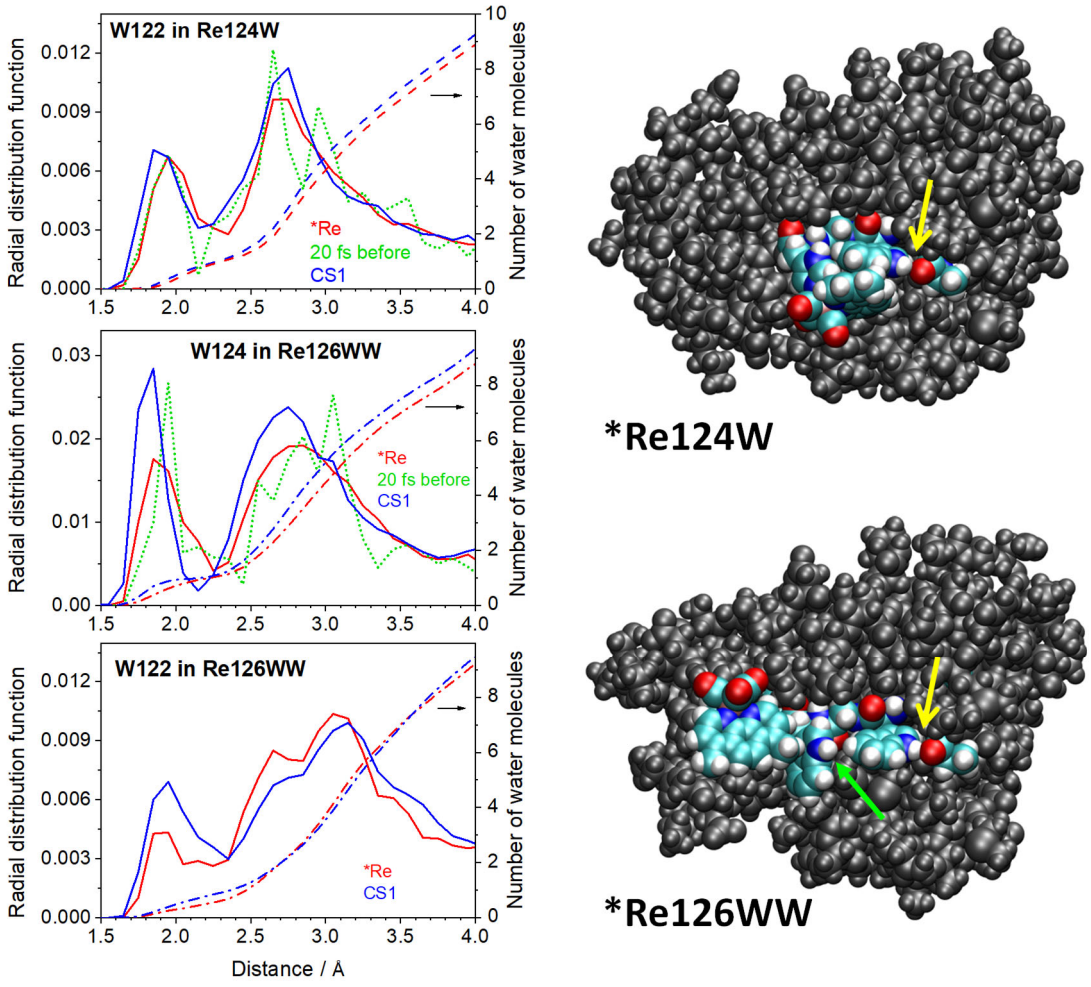

Fig. 5. Left: Water proximal radial distribution function g(*r*) around W122 indole in **Re124W** (top), W124 in **Re126WW** (middle) and W122 in **Re126WW** (bottom) averaged over full-length TDDFT trajectories before (red) and after (blue) *Re/CS1 crossing; dashed-dotted curves are the corresponding integrals. Green dotted curves: g(*r*) averaged over 20 fs before *Re/CS1 crossing. Top-right: a space-filling model of ***Re124W** shows $Re(CO)_3$(dmp) and the W122 indole half-buried in the protein and indole NH in close contact with O(A119) indicated by the yellow arrow. The indole plane faces dmp from one side. Bottom-right: In ***Re126WW**, the dmp ligand is water-exposed and W124-indole protrudes into the solvent (green arrow). W122 indole NH is in a close contact with O(A119). Snapshots taken from *Re MM trajectories (Fig. 2 – top) at 11500 and 24600 ps, respectively.

Electrostatic potential. Environmental effects were monitored in real time by calculating the electrostatic potential at the indoles (φ(W)) and the Re(imidazole)$(CO)_3$(dmp) complex (φ(Re)) generated by all water molecules (φ_{H2O}), the whole classical part (protein+water, φ_{MM}), or the full system including the rest of the QM space (φ is defined in *SI Appendix*, Fig. S23 and section S13.4). We found that decreasing the negative potential at the proximal indole and increasing the potential at the Re complex facilitated system evolution toward the *Re/CS1 crossing. This behavior is attributable to electrostatic stabilization of the positive indole and negative dmp charges in CS1, in combination with *Re destabilization when φ(Re) at the positively charged Re complex increased. φ-variations appeared to be mainly a collective effect arising from a solvation shell shared between the Re complex and the close-lying indole. Upon crossing, CS1 was instantaneously stabilized electrostatically by short-range electron-hole interactions between $Re^{I}(dmp^{\bullet-})$ and $indole^{\bullet+}$. Solvent restructuring and polarization contributed less and took up to 600 fs to develop.

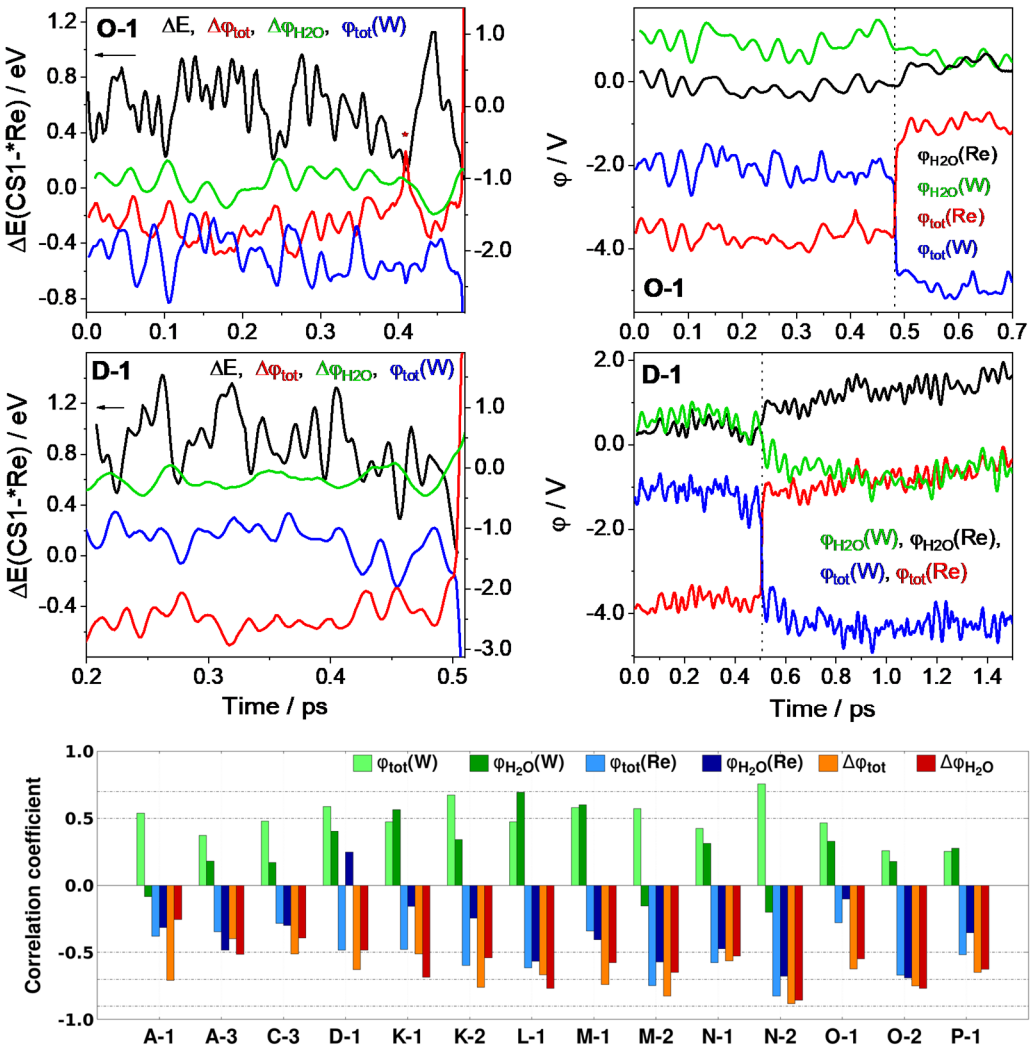

Fig. 6. Left column: Time evolution of the CS1–*Re energy difference ΔE (black, left axis), potential difference $\Delta\varphi = \varphi(\text{Re}) - \varphi(\text{W})$ (W = proximal indole, $\Delta\varphi_{tot}$ in red, $\Delta\varphi_{H2O}$ in green), and $\varphi_{tot}(\text{W})$ (blue) calculated along typical trajectories O-1 (**Re124W**) and D-1 (**Re126WW**) up to the *Re/CS1 crossing. Right: trajectories of φ_{tot} (red, blue) and φ_{H2O} (black, green) at the Re complex and the proximal indole before and after *Re/CS1 crossing (marked by vertical dotted lines). Bottom histogram: Correlation coefficients between time evolutions of ΔE and $\Delta\varphi_{tot}$, $\varphi_{tot}(\text{Re})$, $\varphi_{tot}(\text{W})$, $\Delta\varphi_{H2O}$, $\varphi_{H2O}(\text{Re})$, and $\varphi_{H2O}(\text{W})$ calculated over individual TDDFT trajectories up to the *Re/CS1 crossing. Positive and negative values are for correlation and anticorrelation, respectively. More trajectories, φ at individual fragments, and correlation coefficient diagrams are shown in *SI Appendix*, Figs. S24-S29.

The differences between the potentials at the Re complex and the proximal indole $\Delta\varphi_x = \varphi(\text{Re})_x - \varphi_x(\text{W})$ (x = tot or H_2O) and between the CS1 and *Re energies ΔE along individual

trajectories are anticorrelated, compare red and black curves in the left column of Fig. 6 and the histogram of correlation coefficients below. Large negative correlation coefficients (–0.7 ($\Delta\varphi_{tot}$) and –0.6 ($\Delta\varphi_{H2O}$), averaged over all trajectories) were observed when calculated over full trajectories lengths (Fig. 6), as well as during the last 100 fs before *Re/CS1 crossing (–0.7 for both $\Delta\varphi_{H2O}$, $\Delta\varphi_{tot}$, *SI Appendix*, Fig. S26). The highest values were often obtained when the ΔE trajectory was shifted by 1-6 fs behind the $\Delta\varphi_{tot}$ trajectory (i.e., φ_{tot} drives, ΔE follows). Correlating φ_{tot}(W) instead of $\Delta\varphi_{tot}$ gave a lower coefficient of 0.5. $\Delta\varphi_{tot}$ temporal evolution largely copied $\Delta\varphi_{H2O}$ whose fluctuations were slightly broader and encompassed more frequent finer $\Delta\varphi_{tot}$ oscillations (originating in fast intramolecular modes, *SI Appendix*, section S12). Importantly, φ_{H2O}(W) and φ_{H2O}(Re) separately correlated with ΔE less, with lower coefficients of 0.3 and –0.4, respectively. The better ΔE correlation with $\Delta\varphi_{H2O}$ than with φ_{H2O}(W) or φ_{H2O}(Re) individually implies a collective effect of fluctuating solvation around *Re···W moieties.

*Re/CS1 crossing was accompanied by a virtually instantaneous rise of φ_{tot}(Re) and nearly coincidental φ_{tot}(dmp), and a concomitant drop of φ_{tot}(W), owing to the emergence of a Re(dmp$^{\bullet-}$)···W$^{\bullet+}$ interaction (right columns of Figs. 6 and *SI Appendix*, Fig. S24). On the other hand, φ_{H2O}(W), φ_{H2O}(Re) and nearly parallel φ_{H2O}(CO) did not exhibit abrupt changes. Instead, they slowly decreased and increased, respectively, during 200-600 fs after the crossing, owing to solvent re-adjustment to the new charge distribution. φ_{H2O}(W122) in **Re126WW** also decreased during ~600 fs after *Re/CS1 crossing (*SI Appendix*, Fig. S29), due to higher water abundance in its vicinity, which also was indicated by a higher g(*r*) (Fig. 5 left bottom). However, φ_{tot}(W122) slightly increased, owing to a positive charge at the neighboring W124$^{\bullet+}$.

Notably, all φ_{MM} trajectories were nearly parallel with φ_{H2O} ones, only shifted lower because of a negative, virtually constant potential generated by protein atoms (*SI Appendix*, Fig. S28). Apparently, protein reorganization does not contribute on the short timescales of TDDFT trajectories.

The second hop in Re126WW. This hop was observed only along the B-3 trajectory (Fig. 4). Whereas strong coupling at three snapshots in the CS1/CS2 crossing region (17, 35, 58 meV) favors fast and possibly adiabatic $W124^{\bullet+}\leftarrow W122$ ET, electrostatic-potential trajectories indicate that gradual water restructuring around W122 in CS1 in the direction of the CS2 product is needed to drive the CS1→CS2 conversion (a rare event exhibited by only one trajectory). Also, the experimentally established (36) CS1→CS2 endergonicity was attributed to weaker W122 (than W124) solvation and weaker coulombic interaction of $Re(dmp^{\bullet-})$ with $W122^{\bullet+}$ in CS2 than with $W124^{\bullet+}$ in CS1.

The W122-indole in **Re126WW** is much less exposed to water than W124 (Fig. 5). In CS1, the first W122 g(*r*) maximum and the corresponding integral are nearly 7× and 2.3× lower for W122 than $W124^{\bullet+}$ (Fig. 5). W122 solvation increases upon its oxidation to $W122^{\bullet+}$ in CS2, owing to a water shift from the second solvation sphere and the W124 vicinity, but it remains low compared to W124, as well as to $W124^{\bullet+}$ in CS1 (*SI Appendix*, Fig. S30). (In the CS1/CS2 region, the $W122^{\bullet+}$ NH group interacts directly with a single H_2O molecule and the A119 oxygen, *SI Appendix*, Fig. S22.)

φ_{H2O}(W122) gradually decreases as the system evolves across the B-3 CS1 region, presumably due to water restructuring. Although this decrease amounts only to ca. 0.33 V, it

could decrease the CS2 energy, allowing the system to reach the CS1/CS2 crossing point. φ_{H2O}(W122) decreases by another ca. 1 V over a ~250 fs period after the crossing, as the solvation responds to W122$^{\bullet+}$ formation, stabilizing the CS2-product. On the contrary, coulombic forces in the QM space result in a net destabilization since Re(dmp$^{\bullet-}$)···W124$^{\bullet+}$ in CS1 is replaced by a weaker Re(dmp$^{\bullet-}$)···W122$^{\bullet+}$ interaction in CS2, which is manifested by a decrease of φ_{tot}(Re) and φ_{tot}(dmp) at CS1/CS2 crossing (*SI Appendix*, Fig. S31-right).

***Re/CS2 crossing.** Several TDDFT trajectories indicated the possibility of a direct *Re(CO)$_3$(dmp)$^+$←W122 ET in **Re126WW**, bypassing the W124$^{\bullet+}$ intermediate. Analysis of typical trajectories A-2 and C-1 suggest that *Re/CS2 crossing is favored by a fortuitous water arrangement around both W122 and W124 indoles. The difference between φ_{tot} at W124 and W122 increases in the course of ~200 (A-2) and 40 fs (C-1) intervals before the crossing, almost entirely due to changes in φ_{H2O}. At the *Re/CS2 crossing, φ_{tot}(W122) becomes lower than φ_{tot}(W124) by 0.6 – 0.8 V, while g(*r*) indicates a small shift of solvating water from W124 to the W122 indole on going from *Re to CS2 (*SI Appendix*, Figs. S32, S33). Although *Re→CS2 conversion occurs along several trajectories, it is uncompetitive with sequential hopping because of weak *Re–CS2 electronic coupling (≤0.3 meV). This drawback could, in principle, be overcome by flickering resonance, whereby *Re, CS1, and CS2 states would be temporarily isoenergetic, enabling ballistic ET (67, 68). Alas, we did not find resonant behavior on A-2 or C-1 energy trajectories before the *Re/CS2 crossing. Instead, CS2 became the lowest triplet state through a rapid series of avoided crossings with CS1 and *Re states (*SI Appendix*, Fig. S34).

Concluding remarks

In agreement with the experimentally established reaction mechanism (Scheme 1), our simulations accord with sequential electron transfer between localized redox sites in **Re126WW**. Importantly, our work suggests ET adiabaticity, indicating that reactive states are driven toward crossings by collective solvent fluctuations around *$Re(CO)_3(dmp)\cdots W$ and W124···W122 moieties, while solvation and coulombic interactions between the Re complex and the indole(s) are major contributors to ET energetics.

The first ET step (*$Re(CO)_3(dmp)^+\leftarrow W$) is facilitated by fluctuations of the *Re excited-state electronic structure from predominantly $Re(CO)_3\rightarrow$dmp ^{3}CT to $\pi\pi^*$(dmp) ^{3}IL. Whereas the excited electron stays localized on the dmp ligand, the hole fluctuates from $Re(CO)_3$ to dmp. *Re/CS1 crossings feature stronger electronic coupling when *Re acquires predominantly ^{3}IL rather than mixed ^{3}CT/^{3}IL character. This behavior is qualitatively rationalized in Fig. 7, showing that ^{3}IL matches the through-space dmp···indole pathway, where ET is facilitated by a shorter effective distance than in a ^{3}CT-type *Re state. Moreover, ET to a predominantly ^{3}CT state would require weakly coupled electron tunneling through a negatively charged dmp ligand or a $Re^{II}\leftarrow dmp^{\bullet-}\leftarrow$indole charge shift (formally a simultaneous double-ET). Indeed, trajectories with a high ^{3}CT contribution at the *Re/CS1 crossing (P-2, B-1, D-3) exhibited the smallest $|H_{ab}|$ values (*SI appendix*, Tables S1, S2). Similar arguments apply to guanine oxidation in DNA with intercalated ^{3}IL-excited $Re(pyridine)(CO)_3(dppz)^+$ (69) and, more generally, to any system where an electron donor interacts directly with a polypyridyl ligand of an electronically excited d^6-metal complex.

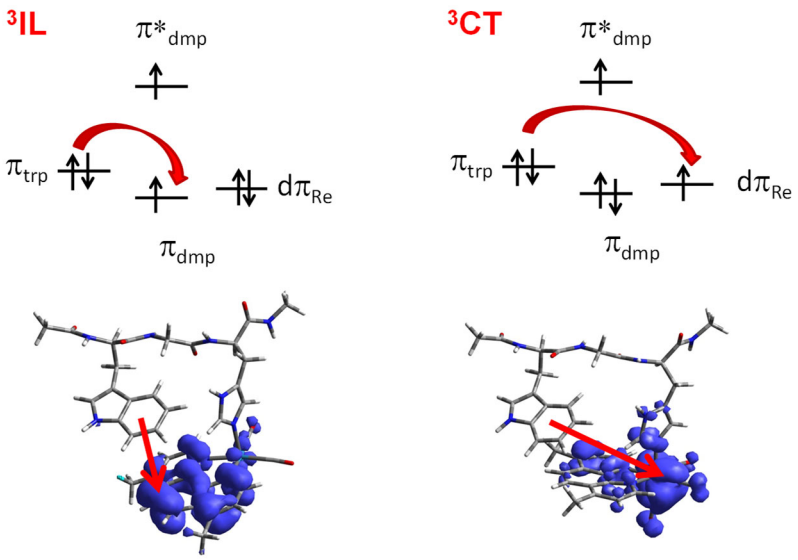

Fig. 7. W122→*Re(H124)$(CO)_3$(dmp)$^+$ ET in ^{3}IL (left) and ^{3}CT (right) states: top, MO diagrams; bottom, hole localization in predominantly ^{3}IL (left) and mixed ^{3}CT/^{3}IL (right) *Re states, calculated as *Re electron detachment densities (70) on snapshots N-1, 1 ps and L-1, 0.25 ps, respectively.

*Re–CS1 and CS1–CS2 electronic couplings are substantial, making Re$(CO)_3$(dmp)$^+$←W ET (also W124$^{\bullet+}$←W122 ET in **Re126WW**) adiabatic, driven by solvation dynamics that bring *Re and CS1 (or CS1 and CS2) states to energetic degeneracy at the crossing points. Considering that comparable coupling values were calculated for interactions between various aromatics and their radical anions or cations (71, 72), as well as between some of the tryptophan and tyrosine residues in enzyme protective pathways (73), it is possible that the more efficient natural redox enzymes combine short-range adiabatic ET steps with nonadiabatic tunneling at longer distances as an additional means of control, depending on coupling magnitudes and environmental dynamics. (Interestingly, electrochemical reduction of cyt *c* attached to gold electrodes by linkers of variable lengths exhibited a switchover from nonadiabatic to a solvent/protein friction-controlled (adiabatic) mechanism at short distances (74, 75).)

Differences in **Re124W/Re126WW** and PL/CRY kinetics are qualitatively attributable to different reaction barriers, as would be expected for adiabatic reactions. Optical excitation of a flavin quinone (FAD) or semiquinone ($FAD^{\bullet-}$) in PL/CRY triggers sequential ET along a conserved tryptophan triad, producing long-range charge separation on a picosecond timescale (10-12, 14, 15, 24). Both flavin $\pi\pi^*$ and $^*Re(CO)_3(dmp)^+$ excited states are electronically coupled with proximal tryptophan indoles by through-space π-interactions between aromatic rings. An average $|H_{ab}|$ of ~7 meV (fluctuating up to 80 meV) was estimated computationally for a plant CRY (76) and 14-15 meV experimentally for a similar flavodoxin (41). Charge separation between the excited chromophore and proximal tryptophan is faster in PL/CRY (0.4-0.8 ps (*FAD) (10, 24) or 30-45 ps ($^*FAD^{\bullet-}$) (11, 12)) than in **Re124W**/ **Re126WW** (~500 ps, Scheme 1). This difference is attributable to a larger driving forces ($-\Delta G^o$) in PL/CRY (–0.7 (*FAD) (10) and –0.4 eV ($^*FAD^{\bullet-}$) (12)) vs. –0.03 eV in **Re124W** (35) that translate to 1300× and 210× larger Franck-Condon factors for *FAD and $^*FAD^{\bullet-}$ redox centers in PL/CRY than in **Re124W**/**Re126WW** (assuming λ = 0.8 eV). Correcting experimental ET rates for different barrier heights leads to comparable preexponential terms for *chromophore←W_1 ET in PL/CRY and Re-azurin systems, supporting the proposed adiabaticity. Hole hopping between indoles in PL/CRY tryptophan triads is a picosecond process where the first ($W_1^{\bullet+}$←W_2) and second ($W_2^{\bullet+}$←W_3) ET steps occur in ≤9 and 30-50 ps, respectively (11, 12, 15, 24); these ET reactions are facilitated in the highly unequilibrated $W_2^{\bullet+}$ solvent environment, which decreases the effective reorganization energy (15, 24, 77, 78). The latter effect is missing in **Re126WW**, where $W124^{\bullet+}$←W122 ET (<3 ns) is energetically uphill and $W124^{\bullet+}$ is relatively long-lived.

Comparing **Re124W**/**Re126WW** with PL/CRY highlights the importance of solvation and water fluctuations in determining the energetics and dynamics of hopping processes. The FADH or FAD chromophore and proximal tryptophan (W_1) are inside the protein core, largely shielded from solvating water, while the second and third tryptophans are progressively more water-exposed. Increasing solvation stabilizes W^+ compared to neutral W, creating a redox-potential gradient that drives the positive charge (hole) along the hopping pathway from the protein interior toward the surface in a series of exergonic ET steps (12, 77-80). Such energy gradient is missing in **Re126WW** where hopping proceeds at a water-exposed protein surface and the second tryptophan (W122) is less accessible to water than the first one (W124). Weaker $W122^{\bullet+}$ solvation and electron-hole interaction with $Re(dmp^{\bullet-})$ in CS2 makes $W124^{\bullet+}\leftarrow W122$ ET endergonic, shifting the CS1/CS2 equilibrium to CS1, where it undergoes unproductive recombination to the ground state (Scheme 1). We conclude that the uphill ET step is the main factor diminishing the Cu^{II} photoproduct yield (Scheme 1, (36)). The situation is very different for PL/CRY, where the terminal $W_3^{\bullet+}$ (being stabilized with respect to $W_2^{\bullet+}$) is produced faster than environmental water relaxation around the $W_2^{\bullet+}$ intermediate.

The solvation gradient along a hopping pathway is the principal factor driving charge separation downhill while increasing water exposure enhances site-energy fluctuations, thereby increasing the probability of electronic-state crossings. Both these features are optimized in PL/CRY to achieve (ultra)fast high-yield charge separation. On the other hand, restricted W122 solvation in **Re126WW** diminishes its performance as a "Cu^{I} photo-oxidase." Increasing the photoproduct yield would require enhancing water access to W122 by modifying the neighboring L120A119S118 α-helix or introducing a negatively charged residue to decrease the

electrostatic potential at W122. We also expect enzyme protective pathways (25, 27, 81) to consist of progressively more solvated tryptophans and tyrosines that are more strongly electronically coupled to each other (73) than to the active site. This differential coupling will ensure efficient charge transport toward the enzyme surface without affecting enzymatic function.

In contrast to tryptophan chains, long-range hopping in multiheme proteins (28, 29) appears to be nonadiabatic, controlled by a delicate balance between driving forces and electronic couplings (30, 31). Cyt *c* cofactors are not directly water-exposed and their formal potentials appear to be controlled by protonations of propionate side chains (82). Although there is no uniform downhill energy gradient along the cyt *c* sequences, endergonic ET steps are still fast, owing to increased electronic couplings. Compared to Re-azurins, heme units are coupled more weakly, $|H_{ab}| < 8$ meV, even when positioned at similar distances (30, 31).

Our simulations suggest that environmental effects on kinetics, thermodynamics and charge-separation yields of hole hopping through tryptophan chains could differ in solutions or in viscous cell interiors or membranes. We expect that hopping will be disfavored in slowly relaxing environments such as glycerol or trehalose solutions, provided that other factors stay constant. Solvent access emerges as a factor to consider when designing protein-based photocatalysts or bioelectronics. In the very interesting cases of electronic conductance in solvent-free protein films (83-87), delocalized electron transport (rather than hopping) is a possible mechanism.

Our work demonstrates that TDDFT-based multiscale QM/MM molecular dynamics simulations of the temporal evolution of low-lying excited-state manifolds can account for

photoinduced ET processes, at least in well-coupled donor-acceptor assemblies in which individual redox states can be treated as electronic excited states of a single reference ground state. We suggest that this computational strategy could be useful for analyses of photoinduced charge separation in other large molecular systems, especially for elucidating molecular aspects of the reaction coordinate and the dependence of protein-mediated coupling on structure and structural fluctuations.

Methods

A detailed description of computational procedures is provided in the *SI Appendix*, section S13. MD simulations of a series of low-lying triplet excited states of **Re124W** and **Re126WW** were performed at QM/MM level in the Terachem 1.9 (88, 89) – Amber 14 (90) framework. The QM part of MD simulations utilized the unrestricted Kohn-Sham approach (UKS) to describe the lowest triplet state and time-dependent DFT (TDDFT) for triplet excited-state manifolds, using the PBE0 functional (91, 92) with a D3 dispersion correction (93). Test calculations with a long-range-corrected functional CAM-B3LYP (94) led to unrealistically large CT-CS energy separations at standard *Re geometries.

In calculating TDDFT/MM/MD, Born-Oppenheimer dynamics were run on the lowest adiabatic triplet state and energies were referenced to the **Re124W** or **Re126WW** singlet ground state. This is a proper reference in the region before the *Re/CS1 crossing but not afterwards, where TDDFT energies dropped unrealistically. Nevertheless, TDDFT/MM/MD charge trajectories were not affected (*SI Appendix*, sections S6 and S13).

*Re–CS1 couplings were calculated by a fragment charge differences method (FCD) (58) at individual points of TDDFT/MM/MD trajectories in Qchem 5.2 software (95) using the PBE0 functional. Test calculations with long-range corrected functionals gave comparable or slightly higher $|H_{ab}|$ values (*SI Apendix*, Tab. S3 and accompanying text). To calculate CS1–CS2 couplings on the B-3 trajectory, we recalculated the adiabatic energies of the lowest CS1 and CS2 states referenced the former, to mitigate the above mentioned reference-state problem.

Unique sets of MM parameters were derived for the ground- and lowest-triplet states of the Re chromophore in a solvated-protein environment, based on atomic charges and equilibrium bond lengths that were calculated separately (QM) for optimized ground- and lowest-triplet $[Re^{I}(im)(CO)_3(dmp)]^+$ structures. Truhlar's CM5 population analysis (96) was used to determine atomic charges instead of the standard RESP procedure (97) that led to an unrealistic (overpolarized) charge distribution at the Re chromophore. Snapshots from *Re excited-state MM/MD trajectories provided initial positions and velocities for subsequent UKS/MM/MD simulations that, in turn, provided initial positions and velocities to calculate final TDDFT/MM/MD trajectories. Essentially, going from MM to UKS enabled ^{3}CT/^{3}IL fluctuations of *Re electronic structure and, hence, charge fluctuations. The solvent responded and its fluctuations made *Re/CS1 crossings possible, possibly aided by high-frequency intramolecular vibrations. (*SI Appendix*, Fig. S35 shows g(*r*) shifting toward W124 in **Re126WW** on going from MM to UKS and then to TDDFT/MM/MD. A possible involvement of intramolecular vibrations is discussed in *SI Appendix*, section S12.) The CS1/CS2 crossing was examined on the trajectory B-3 without preceding MM and UKS steps. Nevertheless, some stabilization of the CS1 geometry occurred on B-3 during the 574 fs following *Re/CS1 crossing.

Our methodology inevitably involved approximations invoked to perform calculations in a realistic time. BO dynamics (and, thus, neglecting nonadiabatic couplings, see above) could limit the description of the state-crossing event (43) itself but it qualitatively well describes the system on approach to the crossing region. Further, our simulations did not involve polarization of surroundings via a polarizable force field and constant atomic charges were used (the only surroundings polarization came from rearrangement of solvent molecules). Our choice of standard unpolarizable force fields was justified by their better and amply-tested description of protein folding.

Acknowledgement

This work was supported by Czech Ministry of Education (MŠMT) grant LTAUSA18026, the EPSRC grant (UK) EP/R029687/1, and the National Institute of Diabetes and Digestive and Kidney Diseases of the National Institutes of Health under award number R01DK019038. The content is solely the responsibility of the authors and does not necessarily represent the official views of the National Institutes of Health. Computational resources were provided by the Czech IT4-Innovations National Supercomputing Center through the MŠMT project, e-Infrastructure CZ – LM2018140“ (OPEN-20-8).

References

1. J. R. Winkler, H. B. Gray, Electron Flow through Metalloproteins. *Chem. Rev.* **114**, 3369−3380 (2014).
2. J. J. Warren, M. E. Ener, A. Vlček, Jr., J. R. Winkler, H. B. Gray, Electron hopping through proteins. *Coord. Chem. Rev.* **256**, 2478-2487 (2012).
3. E. C. Minnihan, D. G. Nocera, J. Stubbe, Reversible, Long-Range Radical Transfer in *E. coli* Class Ia Ribonucleotide Reductase. *Acc. Chem. Res.* **46**, 2524–2535 (2013).

4. B. M. Sjöberg, P. Reichard, Nature of the free radical in ribonucleotide reductase from *Escherichia coli*. *J. Biol. Chem.* **252**, 536-541 (1977).
5. L. Olshansky, J. Stubbe, D. G. Nocera, Charge-Transfer Dynamics at the α/β Subunit Interface of a Photochemical Ribonucleotide Reductase. *J. Am. Chem. Soc.* **138**, 1196−1205 (2016).
6. L. Olshansky, B. L. Greene, C. Finkbeiner, J. Stubbe, D. G. Nocera, Photochemical Generation of a Tryptophan Radical within the Subunit Interface of Ribonucleotide Reductase. *Biochemistry* **55**, 3234−3240 (2016).
7. A. Ehrenberg, P. Reichard, Electron Spin Resonance of the Iron-containing Protein B2 from Ribonucleotide Reductase. *J. Biol. Chem.* **247**, 3485-3488 (1972).
8. A. Sancar, Structure and Function of DNA Photolyase and Cryptochrome Blue-Light Photoreceptors. *Chem. Rev.* **103**, 2203-2237 (2003).
9. Z. Liu *et al.*, Dynamics and mechanism of cyclobutane pyrimidine dimer repair by DNA photolyase. *Proc. Natl. Acad. Sci. USA* **108**, 14831–14836 (2011).
10. Z. Liu *et al.*, Determining complete electron flow in the cofactor photoreduction of oxidized photolyase. *Proc. Natl. Acad. Sci. U.S.A.* **110**, 12966–12971 (2013).
11. A. Lukacs, A. P. M. Eker, M. Byrdin, K. Brettel, M. H. Vos, Electron Hopping through the 15 Å Triple Tryptophan Molecular Wire in DNA Photolyase Occurs within 30 ps. *J. Am. Chem. Soc.* **130**, 14394-14395 (2008).
12. M. Byrdin *et al.*, Quantum Yield Measurements of Short-Lived Photoactivation Intermediates in DNA Photolyase: Toward a Detailed Understanding of the Triple Tryptophan Electron Transfer Chain. *J. Phys. Chem. A* **114**, 3207–3214 (2010).
13. P. Müller, J. Yamamoto, R. Martin, S. Iwai, K. Brettel, Discovery and functional analysis of a 4th electron-transferring tryptophan conserved exclusively in animal cryptochromes and (6-4) photolyases. *Chem. Commun.* **51**, 15502-15505 (2015).
14. P. Müller, E. Ignatz, S. Kiontke, K. Brettel, L.-O. Essen, Sub-nanosecond tryptophan radical deprotonation mediated by a protein-bound water cluster in class II DNA photolyases. *Chem. Sci.* **9**, 1200-1212 (2018).
15. F. Lacombat *et al.*, Delocalized hole transport coupled to sub-ns tryptophanyl deprotonation promotes photoreduction of class II photolyases. *Phys. Chem. Chem. Phys.* **20**, 25446- (2018).
16. N. Jiang *et al.*, Distance-Independent Charge Recombination Kinetics in Cytochrome *c*−Cytochrome *c* Peroxidase Complexes: Compensating Changes in the Electronic Coupling and Reorganization Energies. *J. Phys. Chem. B* **117**, 9129−9141 (2013).
17. B. M. Hoffman *et al.*, Differential influence of dynamic processes on forward and reverse electron transfer across a protein–protein interface. *Proc. Natl. Acad. Sci. USA* **102**, 3564–3569 (2005).
18. J. L. Seifert, T. D. Pfister, J. M. Nocek, Y. Lu, B. M. Hoffman, Hopping in the Electron-Transfer Photocycle of the 1:1 Complex of Zn-Cytochrome c Peroxidase with Cytochrome c. *J. Am. Chem. Soc.* **127**, 5750-5751 (2005).
19. N. A. Tarboush *et al.*, Mutagenesis of tryptophan199 suggests that hopping is required for MauG-dependent tryptophan tryptophylquinone biosynthesis. *Proc. Natl. Acad. Sci. U.S.A.* **108**, 16956–16961 (2011).
20. H. B. Gray, J. R. Winkler, The Rise of Radicals in Bioinorganic Chemistry. *Isr. J. Chem.* **56**, 640–648 (2016).
21. O. Farver, I. Pecht, Electron transfer in blue copper proteins. *Coord. Chem. Rev.* **255**, 757–773 (2011).
22. A. Gupta *et al.*, Involvement of Tyr108 in the Enzyme Mechanism of the Small Laccase from *Streptomyces coelicolor*. *J. Am. Chem. Soc.* **134**, 18213−18216 (2012).

23. C. Wittekindt, M. Schwarz, T. Friedrich, T. Koslowski, Aromatic Amino Acids as Stepping Stones in Charge Transfer in Respiratory Complex I: An Unusual Mechanism Deduced from Atomistic Theory and Bioinformatics. *J. Am. Chem. Soc.* **131**, 8135-8140 (2009).
24. F. Lacombat *et al.*, Ultrafast Oxidation of a Tyrosine by Proton-Coupled Electron Transfer Promotes Light Activation of an Animal-like Cryptochrome. *J. Am. Chem. Soc.* **141**, 13394−13409 (2019).
25. H. B. Gray, J. R. Winkler, Hole hopping through tyrosine/tryptophan chains protects proteins from oxidative damage. *Proc. Natl. Acad. Sci. U.S.A.* **112**, 10920–10925 (2015).
26. J. R. Winkler, H. B. Gray, Electron flow through biological molecules: does hole hopping protect proteins from oxidative damage? *QRB Discovery* **48**, 411–420 (2015).
27. J. R. Winkler, H. B. Gray, Long-Range Electron Tunneling. *J. Am. Chem. Soc.* **136**, 2930−2939 (2014).
28. J. Blumberger, Electron transfer and transport through multi-heme proteins: recent progress and future directions. *Curr. Opin. Chem. Biol.* **47**, 24–31 (2018).
29. J. H. van Wonderen *et al.*, Ultrafast Light-Driven Electron Transfer in a Ru(II)tris(bipyridine)-Labeled Multiheme Cytochrome. *J. Am. Chem. Soc.* **141**, 15190−15200 (2019).
30. X. Jiang *et al.*, Which Multi-Heme Protein Complex Transfers Electrons More Efficiently? Comparing MtrCAB from Shewanella with OmcS from Geobacter. *J. Phys. Chem. Lett.* **11**, 9421−9425 (2020).
31. M. Breuer, K. M. Rosso, J. Blumberger, Electron flow in multiheme bacterial cytochromes is a balancing act between heme electronic interaction and redox potentials. *Proc. Natl. Acad. Sci. U.S.A.* **111**, 111 (2014).
32. T. Hayashi, A. A. Stuchebrukhov, Electron tunneling in respiratory complex I. *Proc. Natl. Acad. Sci. U.S.A.* **107**, 19157–19162 (2010).
33. J. Hirst, M. M. Roessler, Energy conversion, redox catalysis and generation of reactive oxygen species by respiratory complex I. *Biochim. Biophys. Acta* **1857**, 872–883 (2016).
34. J. Fritsch *et al.*, The crystal structure of an oxygen-tolerant hydrogenase uncovers a novel iron-sulphur centre. *Nature* **479**, 249-253 (2011).
35. C. Shih *et al.*, Tryptophan-Accelerated Electron Flow Through Proteins. *Science* **320**, 1760-1762 (2008).
36. K. Takematsu *et al.*, Two Tryptophans are Better than One in Accelerating Electron Flow Through a Protein. *ACS Cent. Sci.* **5**, 192−200 (2019).
37. A. M. Blanco-Rodríguez *et al.*, Phototriggering Electron Flow through Re^{I}-modified *Pseudomonas aeruginosa* Azurins. *Chem. Eur. J.* **17**, 5350 – 5361 (2011).
38. K. Takematsu *et al.*, Hole Hopping Across a Protein-Protein Interface. *J. Phys. Chem. B* **123**, 1578−1591 (2019).
39. S. Mai *et al.*, Competing ultrafast photoinduced electron transfer and intersystem crossing of $[Re(CO)_3(Dmp)(His124)(Trp122)]^+$ in Pseudomonas aeruginosa azurin: a nonadiabatic dynamics study. *Theor. Chem. Acc.* **139**, 65 (2020).
40. A. El Nahhas *et al.*, Ultrafast Excited-State Dynamics of Rhenium(I) Photosensitizers $[Re(Cl)(CO)_3(N,N)]$ and $[Re(imidazole)(CO)_3(N,N)]^+$: Diimine Effects. *Inorg. Chem.* **50**, 2932–2943 (2011).
41. M. Kundu, T.-F. He, Y. Lu, L. Wang, D. Zhong, Short-Range Electron Transfer in Reduced Flavodoxin: Ultrafast Nonequilibrium Dynamics Coupled with Protein Fluctuations. *J. Phys. Chem. Lett.* **9**, 2782−2790 (2018).
42. T.-F. He *et al.*, Femtosecond Dynamics of Short-Range Protein Electron Transfer in Flavodoxin. *Biochemistry* **52**, 9120−9128 (2013).

43. T. Kubař, M. Elstner, A hybrid approach to simulation of electron transfer in complex molecular systems. *J. R. Soc. Interface* **10**, 20130415 (2013).
44. M. D. Newton, Quantum Chemical Probes of Electron Transfer Kinetics: The Nature of Donor-Acceptor Interactions. *Chem. Rev.* **91**, 767-792 (1991).
45. J. Blumberger, Recent Advances in the Theory and Molecular Simulation of Biological Electron Transfer Reactions. *Chem. Rev.* **115**, 11191−11238 (2015).
46. A. Vlček, Jr., Ultrafast Excited-State Processes in Re(I) Carbonyl-Diimine Complexes: From Excitation to Photochemistry. *Top. Organomet. Chem.* **29**, 73-114 (2010).
47. A. Cannizzo *et al.*, Femtosecond Fluorescence and Intersystem Crossing in Rhenium(I) Carbonyl-Bipyridine Complexes *J. Am. Chem. Soc.* **130**, 8967-8974 (2008).
48. A. M. Blanco-Rodríguez *et al.*, Relaxation Dynamics of $[Re^{I}(CO)_3(phen)(HisX)]^+$ (X = 83, 107, 109, 124, 126) *Pseudomonas aeruginosa* Azurins. *J. Am. Chem. Soc.* **131**, 11788-11800 (2009).
49. S. Mai, L. González, Unconventional Two-Step Spin Relaxation Dynamics of $[Re(CO)_3(im)(phen)]^+$ in Aqueous Solution. *Chem. Sci.* **10**, 10405–10411 (2019).
50. S. Mai *et al.*, Excited States of a Rhenium Carbonyl Diimine Complex: Solvation Models, Spin–Orbit Coupling, and Vibrational Sampling Effects. *Phys. Chem. Chem. Phys.* **19**, 27240-27250 (2017).
51. S. Mai *et al.*, Quantitative Wave Function Analysis for Excited States of Transition Metal Complexes. *Coord. Chem. Rev.* **361**, 74–97 (2018).
52. H. Sumi, R. A. Marcus, Dynamical effects in electron transfer reactions. *J. Chem. Phys.* **84**, 4894-4914 (1986).
53. H. Sumi, "Adiabatic versus Non-Adiabatic Electron Transfer" in Electron Transfer in Chemistry. Vol 1., V. Balzani, Ed. (Wiley-VCH, Weinheim, 1999), pp. 64-108.
54. J. N. Onuchic, D. N. Beratan, J. J. Hopfield, Some Aspects of Electron-Transfer Reaction Dynamics. *J. Phys. Chem.* **90**, 3707-3721 (1986).
55. I. Rips, J. Jortner, Dynamic solvent effects on outer-sphere electron transfer. *J. Chem. Phys.* **87**, 2090-2104 (1987).
56. R. J. Cave, M. D. Newton, Generalization of the Mulliken-Hush treatment for the calculation of electron transfer matrix elements. *Chem. Phys. Lett.* **249**, 15-19 (1996).
57. R. J. Cave, M. D. Newton, Calculation of electronic coupling matrix elements for ground and excited state electron transfer reactions: Comparison of the generalized Mulliken–Hush and block diagonalization methods. *J. Chem. Phys.* **106**, 9213-9226 (1997).
58. A. A. Voityuk, N. Rösch, Fragment charge difference method for estimating donor–acceptor electronic coupling: Application to DNA π-stacks. *J. Chem. Phys.* **117**, 5607-5516 (2002).
59. K. Takematsu *et al.*, Tryptophan-Accelerated Electron Flow Across a Protein-Protein Interface. *J. Am. Chem. Soc.* **135**, 15515−15525 (2013).
60. H. Oberhofer, K. Reuter, J. Blumberger, Charge Transport in Molecular Materials: An Assessment of Computational Methods. *Chem. Rev.* **117**, 10319−10357 (2017).
61. M. Bixon, J. Jortner, Solvent relaxation dynamics and electron transfer. *Chem. Phys.* **176**, 467-481 (1993).
62. P. Pospíšil *et al.*, Light-Induced Nanosecond Relaxation Dynamics of RheniumLabeled *Pseudomonas aeruginosa* Azurins. *J. Phys. Chem. B* **124**, 788−797 (2020).
63. J. Polák, D. Ondo, J. Heyda, Thermodynamics of N-Isopropylacrylamide in Water: Insight from Experiments, Simulations, and Kirkwood−Buff Analysis Teamwork. *J. Phys. Chem. B* **124**, 2495−2504 (2020).
64. B. Lin, B. M. Pettitt, On the universality of proximal radial distribution functions of proteins. *J. Chem. Phys.* **134**, 106101 (2011).

65. E. Tang, D. Di Tommaso, N. H. de Leeuw, Hydrogen transfer and hydration properties of HnPO43−n (n = 0–3) in water studied by first principles molecular dynamics simulations. *J. Chem. Phys.* **130**, 234502 (2009).
66. M.-P. Gaigeot, M. Sprik, Ab Initio Molecular Dynamics Study of Uracil in Aqueous Solution. *J. Phys. Chem. B* **108**, 7458-7467 (2004).
67. Y. Zhang, C. Liu, A. Balaeff, S. S. Skourtis, D. N. Beratan, Biological charge transfer via flickering resonance. *Proc. Natl. Acad. Sci. U.S.A.* **111**, 10049–10054 (2014).
68. D. N. Beratan *et al.*, Charge Transfer in Dynamical Biosystems, or The Treachery of (Static) Images. *Acc. Chem. Res.* **48**, 474−481 (2015).
69. E. D. Olmon *et al.*, Charge Photoinjection in Intercalated and Covalently Bound $[Re(CO)_3(dppz)(py)]^+$ - DNA Constructs Monitored by Time-Resolved Visible and Infrared Spectroscopy. *J. Am. Chem. Soc.* **133**, 13718–13730 (2011).
70. M. Head-Gordon, A. M. Grańa, D. Maurice, C. A. White, Analysis of Electronic Transitions as the Difference of Electron Attachment and Detachment Densities. *J. Phys. Chem.* **99**, 14261-14270 (1995).
71. A. Kubas *et al.*, Electronic couplings for molecular charge transfer: Benchmarking CDFT, FODFT, and FODFTB against high-level ab initio calculations. *J. Chem. Phys.* **140**, 104105 (2014).
72. A. Kubas *et al.*, Electronic couplings for molecular charge transfer: benchmarking CDFT, FODFT and FODFTB against high-level ab initio calculations. II. *Phys. Chem. Chem. Phys.* **17**, 14342-14354 (2015).
73. N. F. Polizzi, A. Migliore, M. J. Therien, D. N. Beratan, Defusing redox bombs? *Proc. Natl. Acad. Sci. U.S.A.* **112**, 10821–10822 (2015).
74. H. Yue *et al.*, On the Electron Transfer Mechanism Between Cytochrome c and Metal Electrodes. Evidence for Dynamic Control at Short Distances. *J. Phys. Chem. B* **110**, 19906-19913 (2006).
75. K. L. Davis *et al.*, Electron-Transfer Kinetics of Covalently Attached Cytochrome c/SAM/Au Electrode Assemblies. *J. Phys. Chem. C* **112**, 6571-6576 (2008).
76. F. Cailliez, P. Müller, M. Gallois, A. de la Lande, ATP Binding and Aspartate Protonation Enhance Photoinduced Electron Transfer in Plant Cryptochrome. *J. Am. Chem. Soc.* **136**, 12974−12986 (2014).
77. P. B. Woiczikowski, T. Steinbrecher, T. Kubař, M. Elstner, Nonadiabatic QM/MM Simulations of Fast Charge Transfer in Escherichia coli DNA Photolyase. *J. Phys. Chem. B* **115**, 9846–9863 (2011).
78. G. Lüdemann, P. B. Woiczikowski, T. Kubař, M. Elstner, T. B. Steinbrecher, Charge Transfer in E. coli DNA Photolyase: Understanding Polarization and Stabilization Effects via QM/MM Simulations. *J. Phys. Chem. B* **117**, 10769−10778 (2013).
79. G. Lüdemann, I. A. Solov'yov, T. Kubař, M. Elstner, Solvent Driving Force Ensures Fast Formation of a Persistent and Well-Separated Radical Pair in Plant Cryptochrome. *J. Am. Chem. Soc.* **137**, 1147−1156 (2015).
80. F. Cailliez, P. Müller, T. Firmino, P. Pernot, A. de la Lande, Energetics of Photoinduced Charge Migration within the Tryptophan Tetrad of an Animal (6−4) Photolyase. *J. Am. Chem. Soc.* **138**, 1904−1915 (2016).
81. R. D. Teo *et al.*, Mapping hole hopping escape routes in proteins. *Proc. Natl. Acad. Sci. U.S.A.* **116 |** 15811–15816 (2019).
82. B. M. Fonseca *et al.*, The tetraheme cytochrome from Shewanella oneidensis MR-1 shows thermodynamic bias for functional specificity of the hemes. *J. Biol. Inorg. Chem.* **14**, 375–385 (2009).
83. I. Ron, I. Pecht, M. Sheves, D. Cahen, Proteins as Solid-State Electronic Conductors. *Acc. Chem. Res.* **43**, 945-953 (2010).

84. J. A. Fereiro *et al.*, Protein Electronics: Chemical Modulation of Contacts Control Energy Level Alignment in Gold-Azurin-Gold Junctions. *J. Am. Chem. Soc.* **140**, 13317−13326 (2018).
85. X. Yu *et al.*, Insights into Solid-State Electron Transport through Proteins from Inelastic Tunneling Spectroscopy: The Case of Azurin. *ACS Nano* **10**, 9955–9963 (2015).
86. C. D. Bostick *et al.*, Protein bioelectronics: a review of what we do and do not know. *Rep. Prog. Phys.* **81**, 026601 (2018).
87. Z. Futera *et al.*, Coherent Electron Transport across a 3 nm Bioelectronic Junction Made of Multi-Heme Proteins. *J. Phys. Chem. Lett.* **11**, 9766−9774 (2020).
88. I. S. Ufimtsev, T. J. Martínez, Quantum Chemistry on Graphical Processing Units. 3. Analytical Energy Gradients and First Principles Molecular Dynamics. *J. Chem. Theor. Comp.* **5**, 2619-2628 (2009).
89. A. V. Titov, I. S. Ufimtsev, N. Luehr, T. J. Martínez, Generating Efficient Quantum Chemistry Codes for Novel Architectures. *J. Chem. Theor. Comp.* **9**, 213-221 (2013).
90. D. A. Case *et al.* (2015) AMBER 2014. (University of California, San Francisco).
91. C. Adamo, G. E. Scuseria, V. Barone, Accurate excitation energies from time-dependent density functionl theory: Assessing the PBE0 model. *J. Chem. Phys.* **111**, 2889-2899 (1999).
92. C. Adamo, V. Barone, Toward reliable density functional methods without adjustable parameters: The PBE0 model. *J. Chem. Phys.* **110**, 6158-6170 (1999).
93. S. Grimme, J. Antony, S. Ehrlich, H. Krieg, A consistent and accurate ab initio parametrization of density functional dispersion correction (DFT-D) for the 94 elements H-Pu. *J. Chem. Phys.* **132**, 154104 (2010).
94. T. Yanai, D. P. Tew, N. C. Handy, A new hybrid exchange-correlation functional using the Coulomb-attenuating method (CAM-B3LYP). *Chem. Phys. Lett.* **393**, 51-57 (2004).
95. Y. Shao *et al.*, Advances in molecular quantum chemistry contained in the Q-Chem 4 program package. *Mol. Phys.* **113**, 184-215 (2015).
96. A. V. Marenich, S. V. Jerome, C. J. Cramer, D. G. Truhlar, Charge Model 5: An Extension of Hirshfeld Population Analysis for the Accurate Description of Molecular Interactions in Gaseous and Condensed Phases. *J. Chem. TheoryComput.* **8**, 527−541 (2012).
97. M. Marazzi, H. Gattuso, M. Fumanal, C. Daniel, A. Monari, Charge transfer vs. charge separated triplet excited states of $[Re^{I}(dmp)(CO)_3(His124)(Trp122)]^+$ in water and in modified *Pseudomonas aeruginosa* azurin protein. *Chem. Eur. J.* **25**, 2519 – 2526 (2019).